

An Eulerian-Eulerian CFD Simulation of Air-Water flow in a Pipe Separator

Eyitayo A. Afolabi¹ and J.G.M Lee²

¹Department of Chemical Engineering, Federal University of Technology, Minna, Nigeria.

²School of Chemical Engineering and Advanced Materials, Newcastle University, Newcastle upon Tyne, UK.

Abstract

This paper presents a three dimensional Computational Fluid Dynamics (CFD) of air-water flow using Eulerian –Eulerian multiphase model and RSM mixture turbulence model to investigate its hydrodynamic flow behaviour in a 30 mm pipe separator. The simulated results are then compared with the stereoscopic PIV measurements at different axial positions. The comparison shows that the velocity distribution can be predicted with high accuracy using CFD. The numerical velocity profiles are also found to be in good qualitative agreement with the experimental measurements. However, there were some discrepancies between the CFD results and the SPIV measurements at some axial positions away from the inlet section. Therefore, the CFD model could provide good physical understanding on the hydrodynamics flow behaviour for air-water in a pipe separator.

1. INTRODUCTION

In the past, the multiphase separation technology used in the oil and gas industry has been based on conventional vessel-type separators which are expensive, heavy and bulky in size. Nowadays, compact separators are widely used as an effective and economical alternative to conventional separators especially in offshore platforms in oil and gas production operations. The compact separator is simpler to operate, more lightweight, has neither moving nor internal parts, requires less floor space, and involves lower capital and operational costs. A cyclone is a device that spins a continuous phase stream to remove entrained dispersed phase (s) by centrifugal force. Generally, the cylindrical cyclone has potential application as a free water knockout system in equipment for the upstream oil and gas production. This includes down-hole, surface (onshore and offshore) and subsea separation. The main application of the three phase cylindrical cyclone is to clean oily water for disposal by reducing oil concentrations to the order of parts per million in effluents.

The Gas-Liquid-Liquid Cylindrical Cyclone (GLLCC) is a compact separator, patented by the University of Tulsa, USA to separate gas-liquid-liquid mixtures [1]. An extensive experimental study and mechanistic modelling conducted by Vasquez [1] on the performance of the three phase cylindrical cyclone concluded that it worked effectively as a free water knock-out device for air-water-oil mixture with high water content and low oil volume. However, the cylindrical cyclone performs as a mixer rather than separator at high velocities. There is no information about the complex multiphase flow behaviour inside the three-phase cylindrical cyclone and this prevents complete confidence in its design. Thus, there is a need for additional research, which the present work seeks to provide. A detailed investigation of hydrodynamic flow behaviour inside a three phase separator will allow the correct prediction of separation performance, which is necessary for appropriate design in all applications.

The emergence of more powerful computers with large storage and high capacity processing facilities has provided the basis whereby computational fluid dynamics (CFD) can be used to predict flow pattern velocity profiles under a wide range of design and operating conditions. This has led to a better understanding of the turbulent flow behaviour in cyclones [2, 3]. There are

several features of cyclone modelling that essentially make turbulent flow in cyclone highly anisotropic and these include:

- (a) High curvature of the average streamlines: This leads to the developments of secondary flows which continue to evolve due to the cylindrical geometry [4].
- (b) High swirl intensity and radial shear: as a result of the tangential inlet, high swirl flow develops shear stress as the fluid moves along the solid boundary [5].
- (c) Adverse pressure gradients and recirculation zones. When any of the outlets are open to the atmosphere, there is a negative pressure difference at the centre of the tube, and this results in the formation of an air core along the cyclone axis [6, 7].

Advances in numerical modelling techniques and computers, have provided engineers with a wide selection of commercially available fluid flow models based on the Navier-Stokes equations to reproduce measured data for a different range of cyclone geometries and flow rates. Most commercial CFD packages offer RANS turbulence models (such as, the $k-\epsilon$ model, the renormalisation group model and the anisotropic Reynolds stress model, RSM) and large eddy simulation to simulate turbulent flow [8]. Earlier researchers advocated that RSM gives the best approximation of the measured velocity profiles and is a good indication of its suitability to model the anisotropic turbulence feature in a cyclone when compared with other RANS models. However, RSM simulation can be inherently unstable and slow. It is therefore better to obtain a solution using the $k-\epsilon$ model before activating the RSM calculation.

In this paper, a CFD package ANSYS FLUENT is used to simulate the unsteady air-water flow in a 30mm ID pipe separator and the 3-D numerical solution results are then compared with the experimental measurements using the Stereoscopic Particle Image Velocimetry technique (SPIV). By comparing the predicted velocity profile against those measured data, the numerical model's ability to describe the flow patterns that occur in the real flow system could be determined, and subsequently validated for use in the optimization study.

1.1 Numerical Simulation of Multiphase Flow

In general, the Euler-Lagrange and the Euler-Euler approaches are often used for the numerical simulation of multiphase flows. In the Euler-Lagrange approach the continuous phase is modelled by solving the time averaged Navier-Stokes equations, while the dispersed phase is solved by tracking a large number of particles, bubbles or droplets through the calculated continuous flow field. A fundamental assumption made in this approach is that the dispersed phase occupies a low volume fraction, which would suggest that the dispersed phase elements are not too close and should be treated as isolated [9,10].

The Euler-Euler approach is based on treating the different phases mathematically as interpenetrating continua. Therefore, the phases share the same volume and penetrate each other in space and exchange mass, momentum and energy. However, a fundamental assumption made in this approach is that the phases mix or separate, and that the dispersed phase occupies a high volume fraction [10, 11]. The high volume fraction suggests that the dispersed phase elements are too close to be treated as isolated. Therefore, the interaction between the multiphase flow and the effect of the secondary phase will be large enough to need accounting for. The three different Euler-Euler multiphase flow models available in the ANSYS-FLUENT code are; the Volume of Fluid, Mixture and Eulerian-Eulerian models. Details of the volume of fluid and mixture multiphase models can be found in a comprehensive description by Cokljat et al; [12] and hence are omitted here.

1.2 Model Equations

1.2.1 The Eulerian model

The Eulerian multiphase model is the most sophisticated of multiphase flow models, and this is because of the strong coupling effect which exists between the continuous and dispersed phases. Its solution is based on a single pressure shared by all phases with continuity, momentum and energy equations solved for each phase. Several interphase drag coefficient functions are available in the Eulerian model, which are appropriate for various types of multiphase regimes. Typically drag coefficient models described in terms of local Reynolds numbers are often used to describe phase coupling through the inter-phase exchange terms.

The phase-average continuity and momentum equations for the phase 'k' read;

$$\frac{\partial}{\partial t}(\bar{\alpha}_k \rho_k) + \nabla \cdot (\bar{\alpha}_k \rho_k \tilde{U}_k) = 0 \quad (1)$$

$$\frac{\partial}{\partial t}(\bar{\alpha}_k \rho_k \tilde{U}_k) + \nabla \cdot (\bar{\alpha}_k \rho_k \tilde{U}_k \otimes \tilde{U}_k) = -(\bar{\alpha}_k \nabla \bar{p}) + \nabla \cdot \tilde{\tau}_k' + [F_{DC} + F_{VM} + F_L] \quad (2)$$

The subscript 'k' is replaced by 'c' for continuous phase or 'd' for dispersed phases. The tilde denotes phase-averaged variables, while the overbar refers to time-averaged values. The phase turbulent stress tensor embodies all fluctuations including the so-called pseudo-turbulence. The drag, virtual mass and lift forces are represented as F_{DC} , F_{VN} and F_L respectively. The drag force and virtual mass force between the continuous and dispersed phases are the only momentum exchange force considered and are defined as:

$$F_{DC} = K_{dc} \left[(\tilde{U}_d - \tilde{U}_c) - \left\{ \frac{\bar{\alpha}_d \overline{U'_d}}{\alpha_d} - \frac{\bar{\alpha}_c \overline{U'_c}}{\alpha_c} \right\} \right] \quad (3)$$

$$F_{VM} = 0.5 \alpha_p \rho_p \left(\frac{d_q \bar{v}_q}{dt} - \frac{d_p \bar{v}_p}{dt} \right) \quad (4)$$

Here K_{dc} is a coefficient representing a characteristic density times an inverse time scale of the dispersed phase. The ANSYS FLUENT model assumes that the particle diameter is much smaller than the inter-particle spacing. Thus, the lift force is not considered negligible. In this study, Schiller-Nauman model (Schiller and Naumann, 1935) was used to calculate the fluid-fluid exchange coefficient. The time-averaged terms represent turbulent dispersion in the momentum equations. Turbulent stresses appearing in the momentum equations is defined by;

$$\tilde{\tau}_k^i = -\bar{\alpha}_k \rho_k \tilde{R}_{k,ij} \quad (5)$$

1.2.2 The mixture turbulence model

In the present work, the volume fraction of the dispersed phase is high enough to ensure that the inter-particle collision is significant. Thus, the dominant process is the influence of the primary and secondary phases. Hence, a mixture turbulence model is sufficient to capture important features of the multiphase turbulent flow within the pipe separator. In order to close the phase-averaged momentum equations, the Reynolds stress need to be solved. The transport equation for the continuous phase Reynolds stresses in the case of the mixture turbulence model reads:

$$\begin{aligned} \frac{\partial}{\partial t}(\bar{\alpha} \rho \tilde{R}_{ij}) + \frac{\partial}{\partial x_k}(\bar{\alpha} \rho \tilde{U}_k \tilde{R}_{ij}) = & -\bar{\alpha} \rho \left(\tilde{R}_{ik} \frac{\partial U_j}{\partial x_k} + \tilde{R}_{jk} \frac{\partial U_i}{\partial x_k} \right) + \frac{\partial}{\partial x_k} \left(\bar{\alpha} \mu \frac{\partial}{\partial x_k} \tilde{R}_{ij} \right) \\ & - \frac{\partial}{\partial x_k} \left[\bar{\alpha} \rho \overline{u'_i u'_j u'_k} \right] + \bar{\alpha} \rho \left(\frac{\partial u_i}{\partial x_j} + \frac{\partial u_j}{\partial x_i} \right) - \bar{\alpha} \rho \tilde{\epsilon}_{ij} \end{aligned} \quad (6)$$

The main assumption behind the mixture turbulence model of the RSM option is that all phases share the same turbulence field. The phase properties and phase velocities are replaced with mixture properties and mixture velocities. For example, the mixture density and velocities are calculated as:

$$\rho_m = \sum_{i=1}^N \bar{\alpha}_i \rho_i \quad (7)$$

$$\tilde{U}_m = \frac{\sum_{i=1}^N \bar{\alpha}_i \rho_i \tilde{U}_m}{\sum_{i=1}^N \bar{\alpha}_i \rho_i} \quad (8)$$

Here, N is the number of phases.

2. NUMERICAL METHODOLOGY

2.1 Model Geometry

The geometry of the pipe separator used in this CFD simulation is shown in Figure 1, and is the same used by Afolabi [13], Afolabi and Lee [14] in the experimental investigation of multiphase flow using Stereoscopic Particle Image Velocimetry technique. The geometry was created using the commercial software, Gambit. The dimensions of the pipe separator used are given in Figure 1 and the inclined inlet designed in such a way that its dimensions gradually reduce to 25% of the cross-sectional area. The numerical solution domain of this geometry corresponds to a dimension of 0.885m, 1.82m and 0.646m in radial, axial and tangential direction respectively.

2.2 Separation Mechanism

The air-water mixture enters the pipe separator through the inclined inlet designed to promote the pre-separation of the gas-liquid mixture. The tangential inlet with reduced area produces a swirling motion in the vertical cylindrical pipe. Due to the differences in density, the centrifugal effect segregates the air-water mixture, thereby allows air to flow upward and leaves through the gas outlet. In addition, water flow to the lower section of the pipe separator and flow out through the water and oil-rich outlets.

2.3 Meshing Scheme

Hexahedral and tetrahedral meshing schemes of a commercial pre-processor, GAMBIT from ANSYS Fluent Inc. were used to mesh the model geometry. The geometry was decomposed into different meshable portions using Boolean operations and splits. The section where the tangential inlet joins the main cyclone body and the area where the water rich outlet joins the main body were both meshed using a tetrahedral mesh type. This mesh type was used because it can be easily adjusted to suit the complex geometry. An unstructured hexahedral mesh type was selected to mesh the rest of the separator, as this was to align easily with flow direction, thereby reducing numerical diffusion when compared with other mesh types such as the tetrahedral [15]. Full resolution of the boundary layer was not necessary due to the fact that most of the turbulence in the cyclone is generated in the core flow [16].

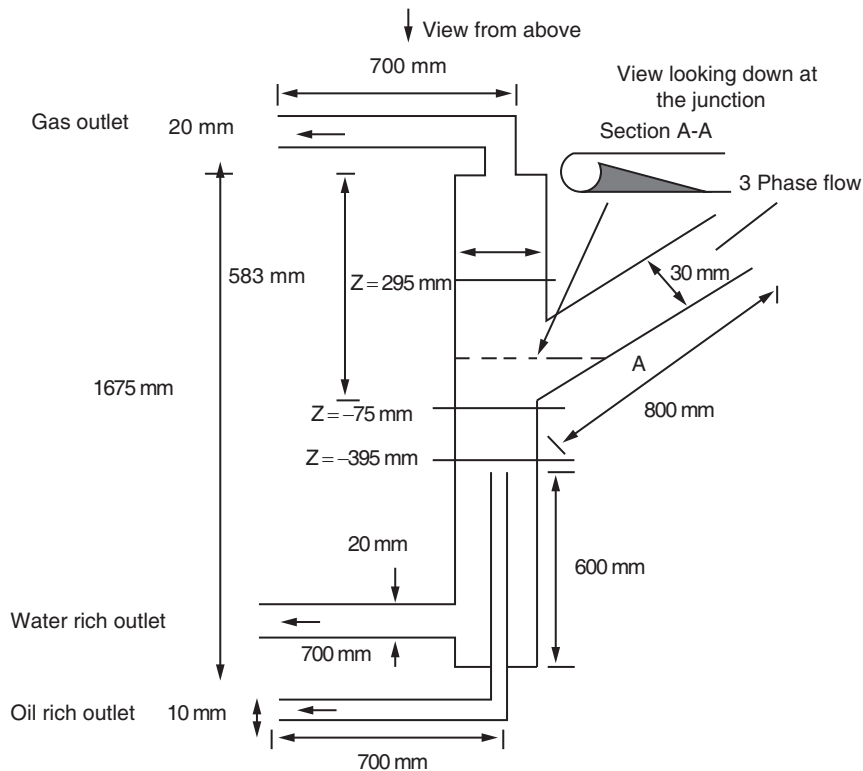


Figure 1. Three-Phase Pipe Separator System.

The three outlets as shown in Figure 1 were all defined as outflows and this was based on the assumption that the diffusion fluxes in the direction normal to the outlet are zero. The tangential inlet was prescribed as a velocity inlet and the rest of the body surfaces (with the exception of the three outlet faces) were treated as solid walls with no slip boundary condition applied. That is, all of the three components of velocity were zero at the wall.

2.4 Numerical Simulation of air-water flow

The grid independence study was conducted with five different grid sizes with cell counts varying from 50,000 to 300,000. This study was carried out by increasing the mesh cells around the inlet section where high turbulence gradients are expected. It was observed that the numerical results obtained became independent of the total number of computational cells beyond 225,000. (i.e grid greater than this produced the results of negligible difference). Therefore, the total number of 225,000 computational cells was selected for the rest of this work.

The Eulerian multiphase model in ANSYS-FLUENT was used to model the air-water multiphase flow in the pipe separator. Here, the primary water phase is treated as a continuum, and air flow is defined as the dispersed phase in the water flow field in the form of bubbles. Data used in this work as boundary conditions is shown in Table 1 and are largely taken from the SPIV measurements of air-water flow with the exact geometry and Reynolds numbers carried out by Afolabi [12].

A segregated, 3-D double precision implicit solver was activated for the simulation of air-water flow inside the 30 mm ID pipe separator. The Cartesian coordinate system was applied with the Phase Coupled SIMPLE (Semi-Implicit Method for Pressure Linked Equations) algorithm for pressure-velocity coupling. In the present work, the volume fraction of the dispersed phase is high enough to ensure that the inter-particle collision is significant. Therefore, the dominant process in the random motion of the mixture turbulence is the influence of the primary and secondary phases. Hence, a RSM mixture turbulence model was used to capture the anisotropic features associated with the turbulent flow within the pipe separator.

The standard wall function [17] was used for the near-wall treatments of the wall boundaries. Operating conditions were specified as being standard atmospheric pressure (101325 Pa) with gravitational acceleration taken as 9.81 m/s^2 and defined to act downwards in the main body of the pipe separator. In this study, the flow through the outlets was specified such that the percentage of fluid as a fraction of the inlet mass flow as shown in Table 1. The outflow boundary condition was chosen for the three outlets since the split ratio can be specified and is expected to influence the flow distribution and the gas concentration within the cyclone.

The following assumptions were used in the Eulerian simulation of air-water flow in a pipe separator:

- The air-water flow in this pipe separator was treated as unsteady, isothermal flow of a viscous, incompressible fluid.
- All of the air phase at the inlet is assumed to move to the top of the cyclone and to pass out through the air outlet.
- The numerical computation ignored droplet/bubble size distributions and used an average sizes obtained from a grade efficiency curve provided by Patterson and Munz [18]. Hence, diameter of air bubbles of $100 \mu\text{m}$ was used for this study.

Table 1. Boundary Condition at the Inlet for Air-Water Experiments

| Gas flow rate ($10^{-5}\text{m}^3/\text{s}$) | Water flow rate ($10^{-4}\text{m}^3/\text{s}$) | Gas volume fraction (%) | Split ratio (water outlet) | Split ratio (air outlet) | Split ratio (oil outlet) |
|---|---|----------------------------|----------------------------------|-----------------------------------|-----------------------------------|
| 4.5 | 2.05 | 18.0 | 0.317 | 0.066 | 0.617 |
| 4.5 | 1.96 | 18.67 | 0.332 | 0.069 | 0.599 |
| 4.5 | 1.85 | 19.57 | 0.352 | 0.072 | 0.576 |
| 4.5 | 1.58 | 22.17 | 0.40 | 0.1 | 0.5 |
| 4.5 | 1.48 | 23.32 | 0.439 | 0.1 | 0.47 |
| 4.5 | 1.32 | 25.42 | 0.48 | 0.11 | 0.41 |

- (d) The boundary conditions for the inflow velocities and volume fractions at the pipe separator inlet were assumed to be uniform.
- (e) No slip boundary condition for which all three components of velocity are identically zero at the wall was used for all numerical simulations in this study.
- (f) The primary and secondary phases move at different velocities. Therefore, the slip velocity equation is solved according to equation 9.

$$\bar{V}_{pq} = \bar{V}_p - \bar{V}_q \quad (9)$$

Where \bar{V}_{pq} is the slip velocity, p and q is primary and secondary phase respectively.

- (g) A single pressure field is shared by all phases;
- (h) Momentum and continuity equations are solved for each phase
- (i) The drag and gravity forces are of significance due to the large water-air density ratio. The Schiller-Naumann model is used to calculate drag coefficient and the gravitational acceleration of 9.81 m/s^2 specified in the operating conditions panel.
- (j) As the default options, wall reflection effects and linear pressure-strain of the RSM multiphase model are applied to the mixture.
- (k) In addition, other factors such as lift, collision, transfer of heat and mass, and surface tension, are neglected [20, 21].

The air-water flow field was pre-established through the unsteady state simulation using the standard $k-\epsilon$ model with the mixture model and this was run for at least 5 seconds before switching to the Eulerian model. A transient solver with a 0.01 seconds time step and convergence criteria of at least 10^{-4} were used. Since the flow field in the pipe separator was found to be highly swirling and anisotropic in nature, the $k-\epsilon$ model solution is then switched to RSM mixture turbulence model. Slack et al; [15] reported that higher order discretization schemes provide better accuracy than first and second order schemes for grids aligned with the flow direction, especially for rotating and swirling flows. However, for the initial simulation, the default first order scheme was used to discretize the momentum, turbulent kinetic energy, dissipation rate and Reynolds stress terms. Thereafter, the QUICK (Quadratic Upwind Interpolation for Convective Kinetic) was used after converging with the second order scheme. In order to ensure that the flow features were fully developed, the transient simulation was run for at least 12 seconds (more than mean residence time of 10 seconds).

3.0. RESULTS AND DISCUSSION

Comparisons are made between the CFD simulation of the air-water flow and the experimental data obtained using the SPIV technique at the three different axial positions.

3.1. Tangential Velocity

A general feature of the comparison between the mean tangential velocity profiles is that the shapes of the experimental and simulated tangential velocity profiles are similar. The tangential velocity profiles indicate that the tangential flow is characterized by a forced- vortex close to the centre and a free vortex-type as we move close to the wall. Studies of the tangential velocity with similar qualitative behaviour have also been done by Bai et al; [22], Bergstrom and Vomhoff [23], Leeuwner and Eksteen [23] and Erdal [24].

Figure 2 (A-C) shows that the CFD simulation under-predicted the tangential velocity profiles moving away from the centre of the tube and over-predicted towards the wall on comparison with the experimental data. For example, Figure 2(B) shows that the measured tangential velocity was 0.29 m/s at $x = -2.5 \text{ mm}$. However, the CFD prediction at this point is 0.25 m/s. Towards the wall; Figure 2(C) shows that the predicted tangential velocity is 0.24 m/s at $x = -10 \text{ mm}$. However, the experimental result at $x = -10 \text{ mm}$ was 0.20 m/s. The predicted tangential velocity profiles in Figure 2 (D-F) generally display good quantitative agreement with experimental results moving close to the centre of the tube. The computed mean tangential velocity profiles agreed to within $\pm 1\%$ for the majority of the measured values at the centre of the tube. However, moving close to the wall, the simulation results are observed to over-predict mean tangential velocity as seen in Figure 3 (C). In the same manner, Figure 3(D-E) show that, close to the wall, the predictions are higher at negative values of the x-axis and lower at positive values.

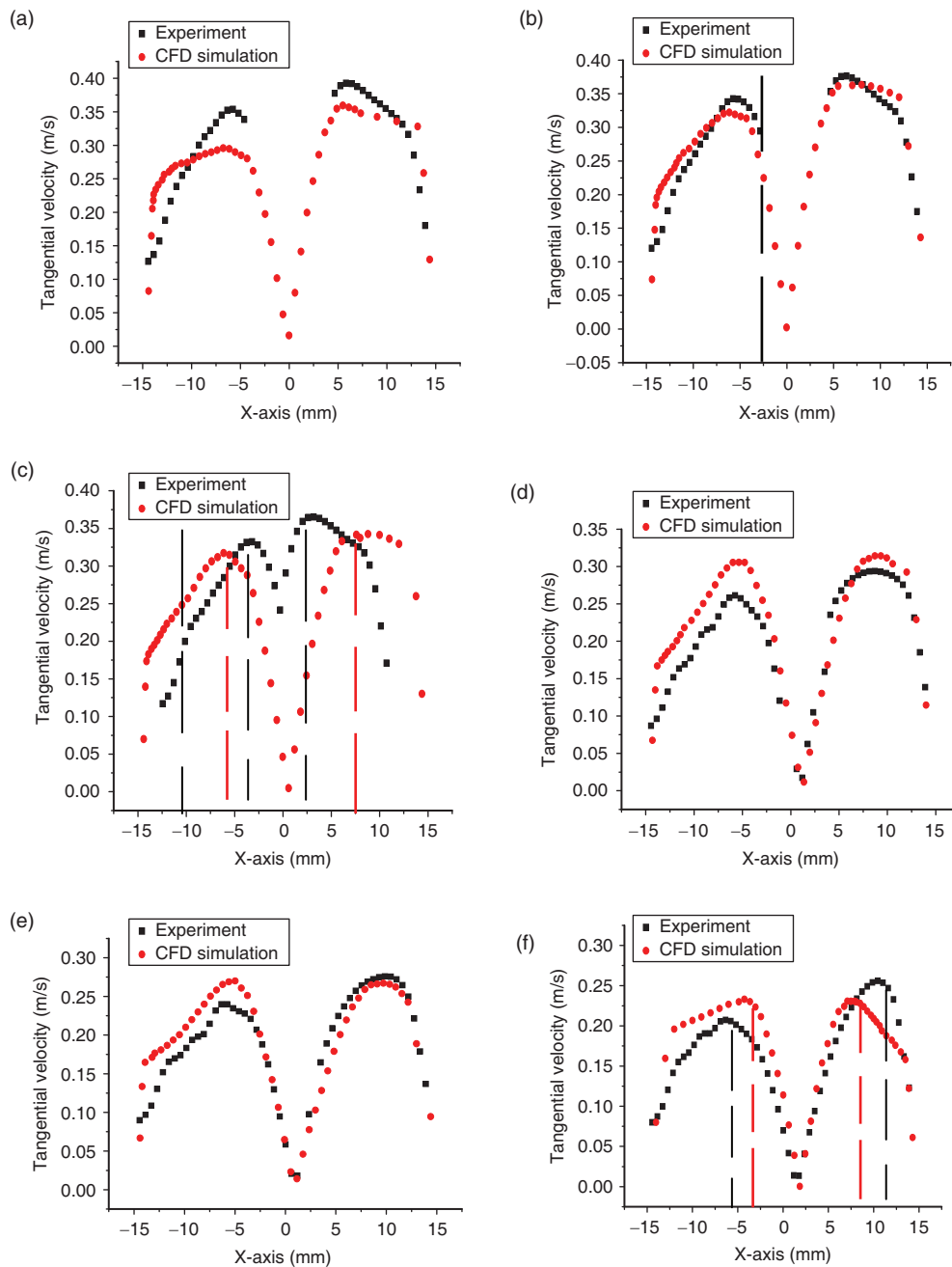


Figure 2. Comparison of the CFD Results with Experimental Data for Mean Tangential Velocity of Air-Water Flow at the Z = -395 mm Axial Position; A: $2.05 \times 10^{-4} \text{ m}^3/\text{s}$ (water), $4.5 \times 10^{-5} \text{ m}^3/\text{s}$ (air); B: $1.96 \times 10^{-4} \text{ m}^3/\text{s}$ (water), $4.5 \times 10^{-5} \text{ m}^3/\text{s}$ (air); C: $1.85 \times 10^{-4} \text{ m}^3/\text{s}$ (water), $4.5 \times 10^{-5} \text{ m}^3/\text{s}$ (air); D: $1.58 \times 10^{-4} \text{ m}^3/\text{s}$ (water), $4.5 \times 10^{-5} \text{ m}^3/\text{s}$ (air); E: $1.48 \times 10^{-4} \text{ m}^3/\text{s}$ (water), $4.5 \times 10^{-5} \text{ m}^3/\text{s}$ (air); F: $1.32 \times 10^{-4} \text{ m}^3/\text{s}$ (water), $4.5 \times 10^{-5} \text{ m}^3/\text{s}$ (air).

The tangential velocity profiles presented in Figures 2 (A-D) and 2 (E-F) shows that free vortex region begins at larger values of the x-axis and at smaller values of the x-axis respectively in the simulation results. For example, Figure 2(C) shows that the maximum tangential velocity from the experimental data occurs at $x = 2.5 \text{ mm}$ and -3.5 mm . However, from the simulation results it occurs at $x = 7.5 \text{ mm}$ and -5.5 mm . Likewise, Figure 2(F) shows that the maximum tangential velocity from the experimental results result occurs at $x = 10.25 \text{ mm}$ and -6.75 mm , whereas in the simulation it occurs at $x = 7.5 \text{ mm}$ and -4.5 mm .

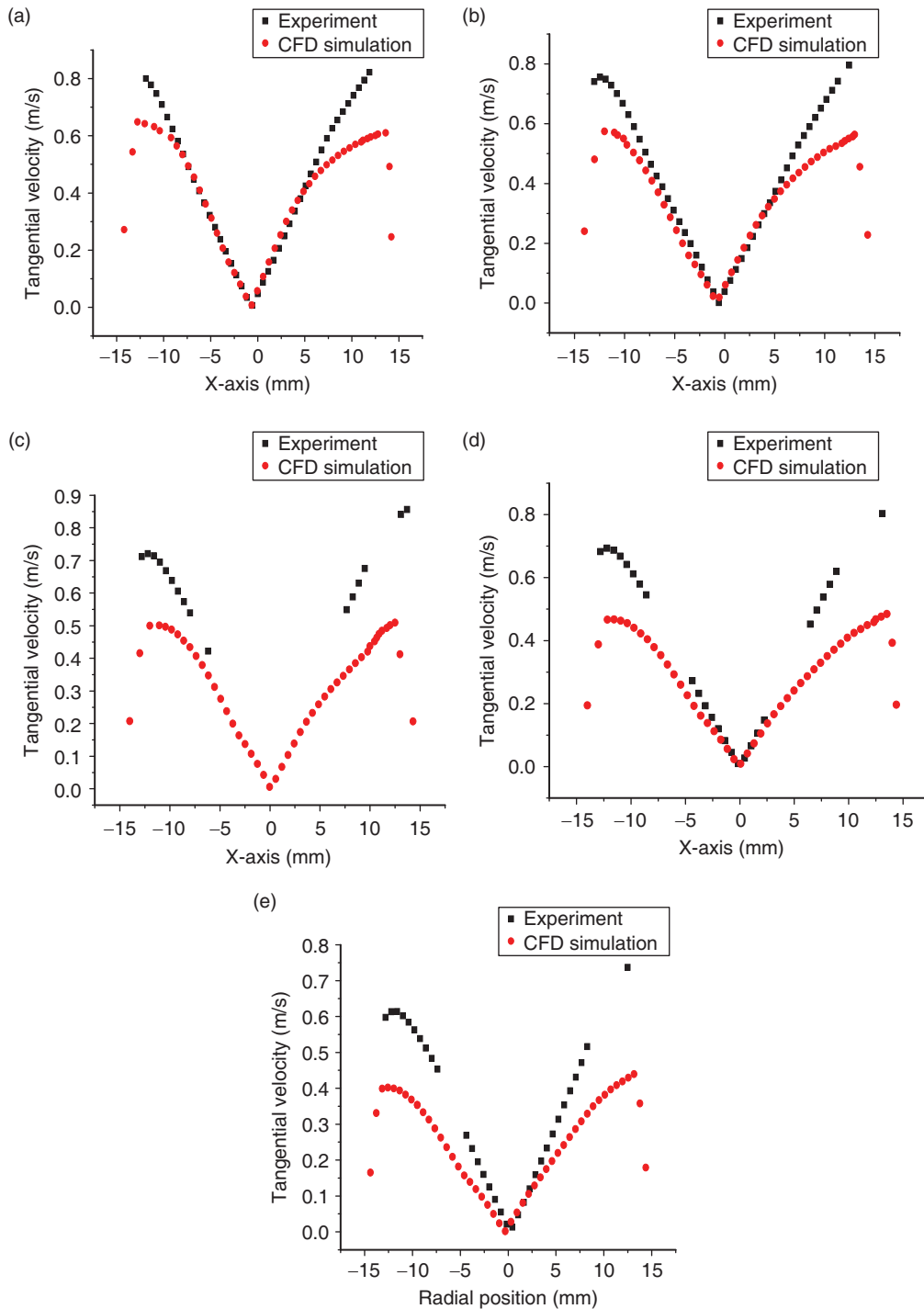


Figure 3. Comparison of the CFD Results with Experimental Data for Mean Tangential Velocity of Air-Water Flow at the $Z = -75$ mm Axial Position; A: $1.96 \times 10^{-4} \text{m}^3/\text{s}$ (water), $4.5 \times 10^{-5} \text{m}^3/\text{s}$ (air); B: $1.85 \times 10^{-4} \text{m}^3/\text{s}$ (water), $4.5 \times 10^{-5} \text{m}^3/\text{s}$ (air); C: $1.58 \times 10^{-4} \text{m}^3/\text{s}$ (water), $4.5 \times 10^{-5} \text{m}^3/\text{s}$ (air); D: $1.48 \times 10^{-4} \text{m}^3/\text{s}$ (water), $4.5 \times 10^{-5} \text{m}^3/\text{s}$ (air); E: $1.32 \times 10^{-4} \text{m}^3/\text{s}$ (water), $4.5 \times 10^{-5} \text{m}^3/\text{s}$ (air).

In Figure 3(A-E), the predicted tangential velocity profiles give good qualitative agreement when compared with the experimental measurements at the centre of the tube. The best agreement occurred at the inner core, $x = \pm 5$ mm, where the prediction was within 5% of the experimental profile for the majority of values of the x-axis at the centre of the tube. However, moving closer to the wall, the simulation is observed to under-predict the tangential velocity. The biggest discrepancy, as shown in

Figure 3 (E) occurred at $x = 10\text{mm}$, where the computational model under-predicted the tangential velocity by 35%. As can be seen in Figure 3 (A-E), the simulated free vortex region begins at the same radius when compared with the experimental data. For example, Figure 3(B) shows that the free vortex region in both the simulation and experimental profiles starts at $x = -11.75\text{ mm}$.

3.2. Axial Velocity

Figures 4 and 5 show the comparison between the mean axial velocity profiles obtained by the CFD simulation and the SPIV measurements. As shown in Figure 4(A), the measured and experimental axial velocity profiles show a downward flow region at all x-axis coordinates. In the same manner, Figures

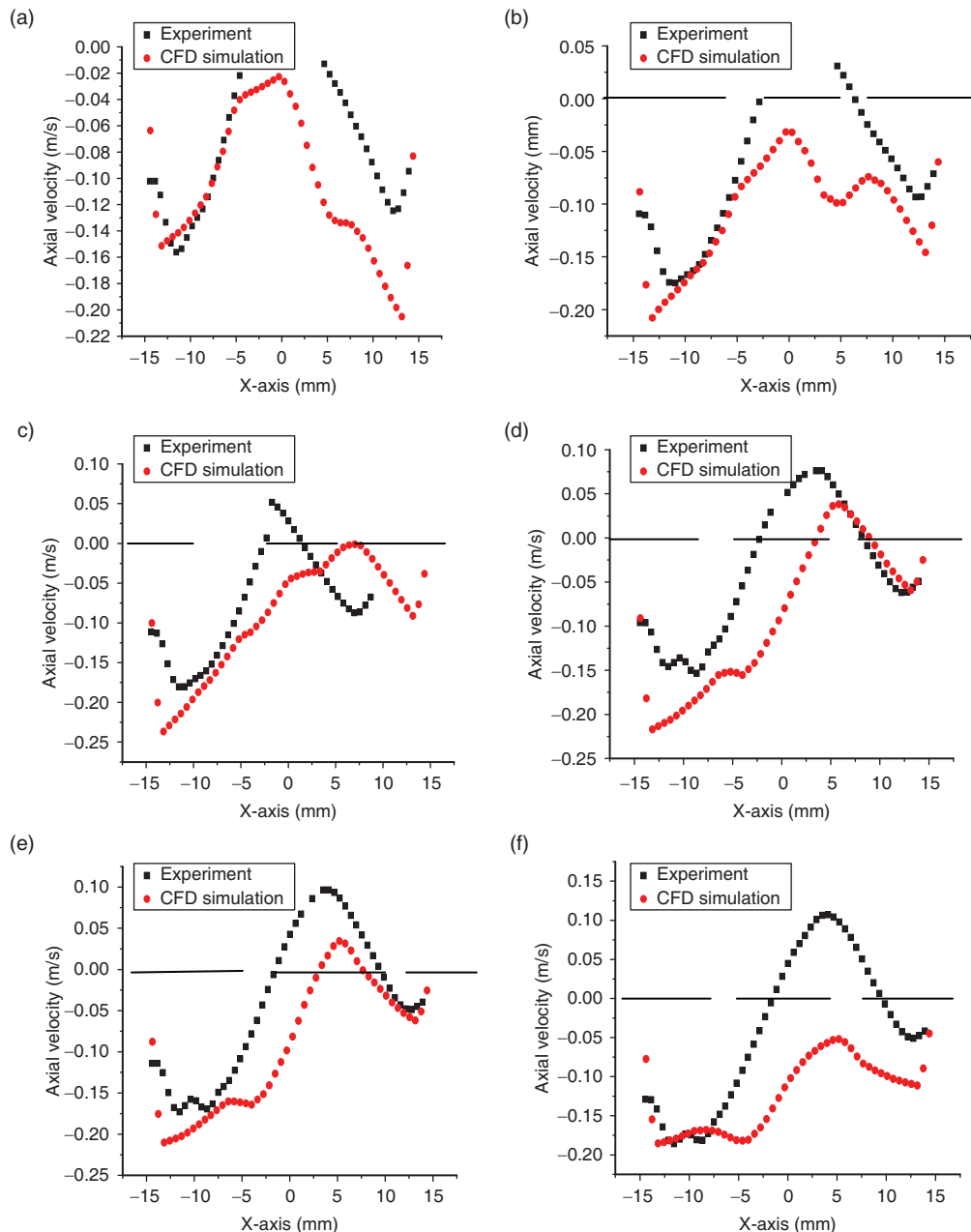


Figure 4. Comparison of the CFD Results and Experimental Data for Mean Axial Velocity of Air-Water Flow at the $Z = -395\text{ mm}$ Axial Position; A: $2.05 \times 10^{-4}\text{m}^3/\text{s}$ (water), $4.5 \times 10^{-5}\text{m}^3/\text{s}$ (air); B: $1.96 \times 10^{-4}\text{m}^3/\text{s}$ (water), $4.5 \times 10^{-5}\text{m}^3/\text{s}$ (air); C: $1.85 \times 10^{-4}\text{m}^3/\text{s}$ (water), $4.5 \times 10^{-5}\text{m}^3/\text{s}$ (air); D: $1.58 \times 10^{-4}\text{m}^3/\text{s}$ (water), $4.5 \times 10^{-5}\text{m}^3/\text{s}$ (air); E: $1.48 \times 10^{-4}\text{m}^3/\text{s}$ (water), $4.5 \times 10^{-5}\text{m}^3/\text{s}$ (air); F: $1.32 \times 10^{-4}\text{m}^3/\text{s}$ (water), $4.5 \times 10^{-5}\text{m}^3/\text{s}$ (air).

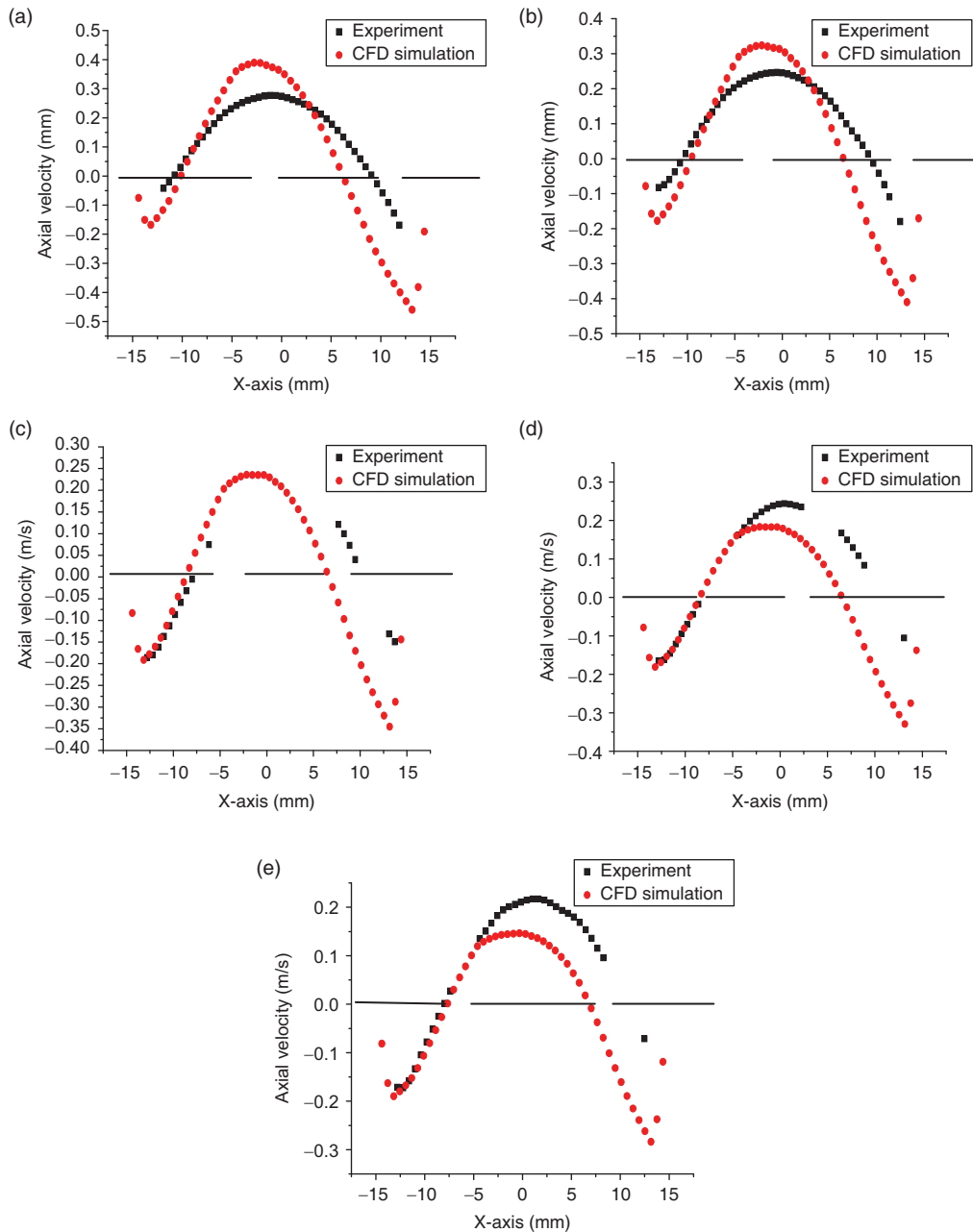


Figure 5. Comparison of the CFD Results and Experimental Data for Mean Axial Velocity of Air-Water Flow at the $Z = -75$ mm Axial Position; A: $1.96 \times 10^{-4} \text{m}^3/\text{s}$ (water), $4.5 \times 10^{-5} \text{m}^3/\text{s}$ (air); B: $1.85 \times 10^{-4} \text{m}^3/\text{s}$ (water), $4.5 \times 10^{-5} \text{m}^3/\text{s}$ (air); C: $1.58 \times 10^{-4} \text{m}^3/\text{s}$ (water), $4.5 \times 10^{-5} \text{m}^3/\text{s}$ (air); D: $1.48 \times 10^{-4} \text{m}^3/\text{s}$ (water), $4.5 \times 10^{-5} \text{m}^3/\text{s}$ (air); E: $1.32 \times 10^{-4} \text{m}^3/\text{s}$ (water), $4.5 \times 10^{-5} \text{m}^3/\text{s}$ (air).

4(B, C and F) show that the predicted axial velocity profiles are mainly of a downward flow region at all x-axis coordinates. However, the measured axial velocity profiles indicate an upward flow pattern at the centre of the tube and a downward flow pattern at the wall. The predicted and measured axial velocity profiles are shown in Figure 4 (D, E), indicating the presence of upward and downward flow regions at the centre of the tube and close to the wall respectively. Therefore, from Figure 4 (B, C and F) the computational model fails to predict the upward flow as observed in the measured axial velocity profiles. This disagreement is due to the effect of natural rubber bungs used in experimental measurements to specify the split ratio as a function of mass flow rate passing through each outlet. The flow direction is expected to have changed as the flow reaches the bung at the outlet.

The axial velocity profiles presented in Figure 4 (A-F) show that the simulation results are generally under-predicted when compared with the experimental data. For example, Figure 4(D) shows that the maximum upward axial velocity for the experimental data is 0.08 m/s, but in the simulation result it is 0.045 m/s. The best correlation between the experimental measurements and the predicted results in Figures 4 (A-C) was obtained close to the wall region at negative values of the x-axis. Here, agreement was within 5-10%. The same trend is obtained as we move close to the wall at positive values of the x-axis, as shown in Figure 4 (D-E). The predicted and measured axial velocity profiles as shown in Figure 5 (A-E) indicate the presence of upward and downward flow regions at the centre of the tube and the wall respectively. As can be seen in Figure 5 (A and B), the predicted axial velocity profile is found to be greater than the experimental data at the centre of the tube. However, as we move close to the wall, the simulation results are found to under-predict when compared with the experimental data. The predicted axial velocities agree with the experimental data in Figure 5 (D-F) to within approximately $\pm 2\%$ as we move from $x = -5$ mm to the wall region at negative values of the x-axis. However, moving from $x = -5$ mm to the wall region at positive values of the x-axis, the simulated profiles are found to under-predict.

3.3. Radial Velocity

Figure 6 (A-B) shows that the computational models give qualitative agreement with the experimental measurements except at wall region at negative values of the x-axis where an inward flow pattern is observed. There is disagreement between the experimental and computational results for Figure 6 (C-F), and they even contradict each other. In Figure 7 (A-E), the predicted and measured radial velocity profiles show an outward flow pattern at all x-axis coordinates. The results demonstrate that ANSYS FLUENT give a good qualitative agreement with measured data at most x-axis coordinates. The experimental and predicted radial velocity profiles show a maximum radial velocity occurring at the centre of the tube and off-centre as shown in Figure 7 (A, B) and (C-E), respectively. However, a better correlation between the experimental measurements and predicted results was obtained close to the wall region of the separator. As can be seen in Figure 7(C-E), the simulation results over-predict at negative values of the x-axis and under-predict at positive values of the x-axis.

The velocity profiles presented so far are restricted to -395mm and -75 mm axial positions. The volume fraction of air distribution in pipe separator was investigated using the CFD simulation at $Z = 295$ mm. Since the main objective of the operation of a pipe separator is the separation of multiphase flows, therefore contour plots of the volume fraction is expected to provide a better insight into the phase distribution within the separator. Figures 8 shows the contours of air volume fractions at $Z = 295$ mm from the CFD simulations of the air-water mixture. The results revealed the presence of air core at the centre of the cross section while the outer part is occupied by water. As can be seen in Figure 8, the magnitude of the air void fraction distribution increases with an increase in the volume fraction of air from 18% to 25%. This confirmed why fewer SPIV data were collected at $Z = 295$ mm as volume fraction of air increases from 18% to 25%. Since the air bubble formed cast a shadow over tracer particles, thereby produced blur images with little or no data.

Figure 9 show the contour plot of air volume fractions for air volume fraction of 0.4 at the inlet. It can be observed that scale of separation increases with the volume fraction of air at the inlet. This can be attributed to an increase in air volume fraction at the inlet that led to an increase in the amount of air flow accumulated at the centre of the tube.

The computational models have produced some very encouraging results for air-water multiphase flow in pipe separator, giving both qualitative and quantitative agreement. However, there were discrepancies and inaccuracies between the CFD and measured results. It is then important to identify limitations of this verification exercise and the antecedent consequences.

- (1) The standard wall function is ineffective when near-wall flows as observed in a pipe separator are subjected to strong body force, severe pressure gradients associated with boundary layer separation, and regions of high curvature. However, resolving a highly swirling flow with small mesh resolution required by enhanced wall approach using the RSM and Eulerian models is found to be too costly and time consuming in terms of computational resources [25, 26].

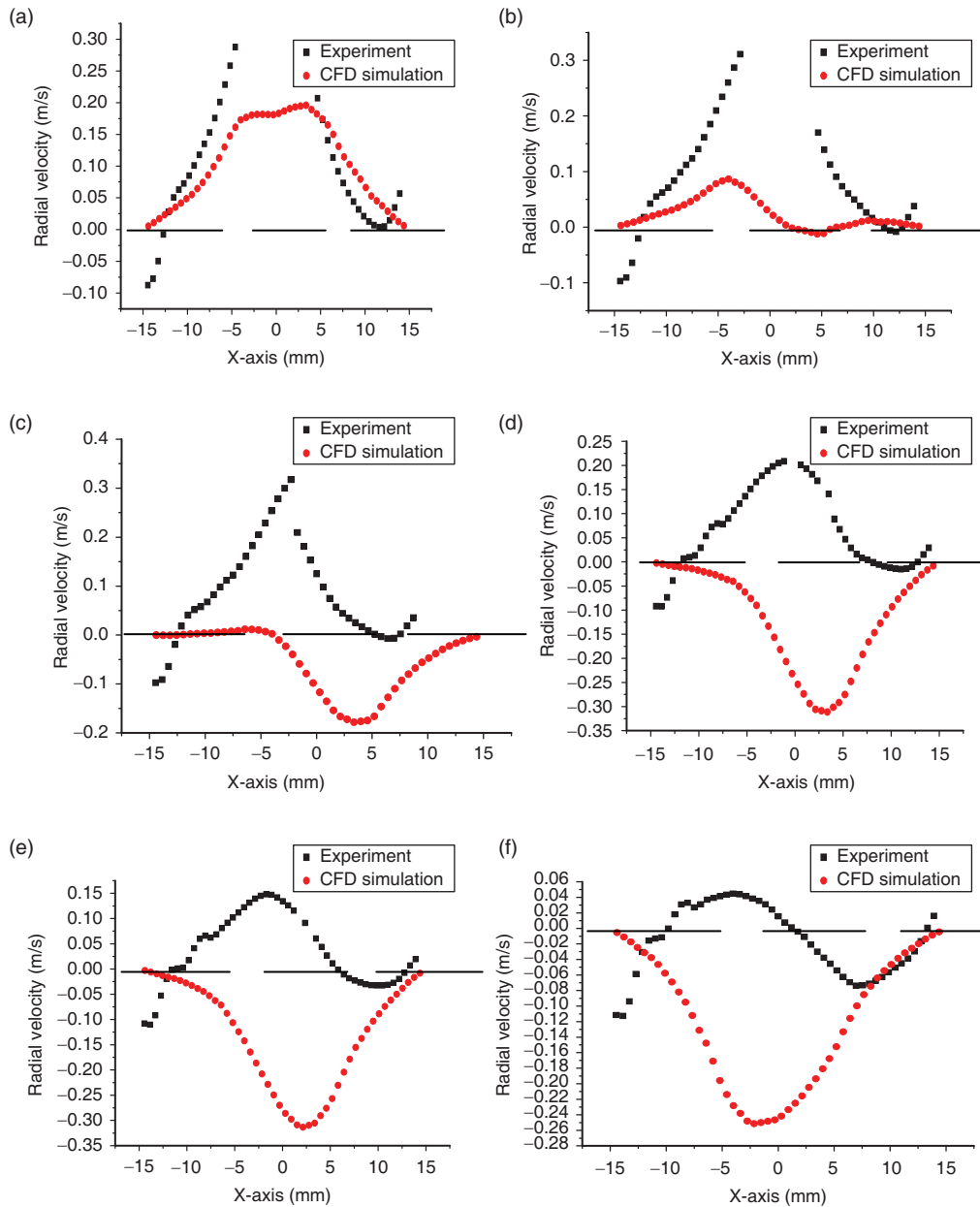


Figure 6. Comparison of the CFD Results and Experimental Data for Mean Radial Velocity of Air-Water Flow at the $Z = -395$ mm Axial Position; A: $2.05 \times 10^{-4} \text{ m}^3/\text{s}$ (water), $4.5 \times 10^{-5} \text{ m}^3/\text{s}$ (air); B: $1.96 \times 10^{-4} \text{ m}^3/\text{s}$ (water), $4.5 \times 10^{-5} \text{ m}^3/\text{s}$ (air); C: $1.85 \times 10^{-4} \text{ m}^3/\text{s}$ (water), $4.5 \times 10^{-5} \text{ m}^3/\text{s}$ (air); D: $1.58 \times 10^{-4} \text{ m}^3/\text{s}$ (water), $4.5 \times 10^{-5} \text{ m}^3/\text{s}$ (air); E: $1.48 \times 10^{-4} \text{ m}^3/\text{s}$ (water), $4.5 \times 10^{-5} \text{ m}^3/\text{s}$ (air); F: $1.32 \times 10^{-4} \text{ m}^3/\text{s}$ (water), $4.5 \times 10^{-5} \text{ m}^3/\text{s}$ (air).

- (2) The Eulerian model used in this work is found to be less computationally stable due to large number of equations involves in its numerical simulation [12]. In this work, bubble or droplet forms of the dispersed phase interact only with the primary phase, neglecting the interactions between bubbles/droplets. However, these interactions cause coalescence and breakage that are proved to generate a considerate influence on the flow pattern in the pipe separator [19].
- (3) Dispersed systems are always more viscous than the pure continuous phase and the more dispersed particles present, the greater the viscosity of the multiphase flow. The Einstein equation [7] describes the magnitude of the effect of dispersed phase on the continuous phase and is given by:

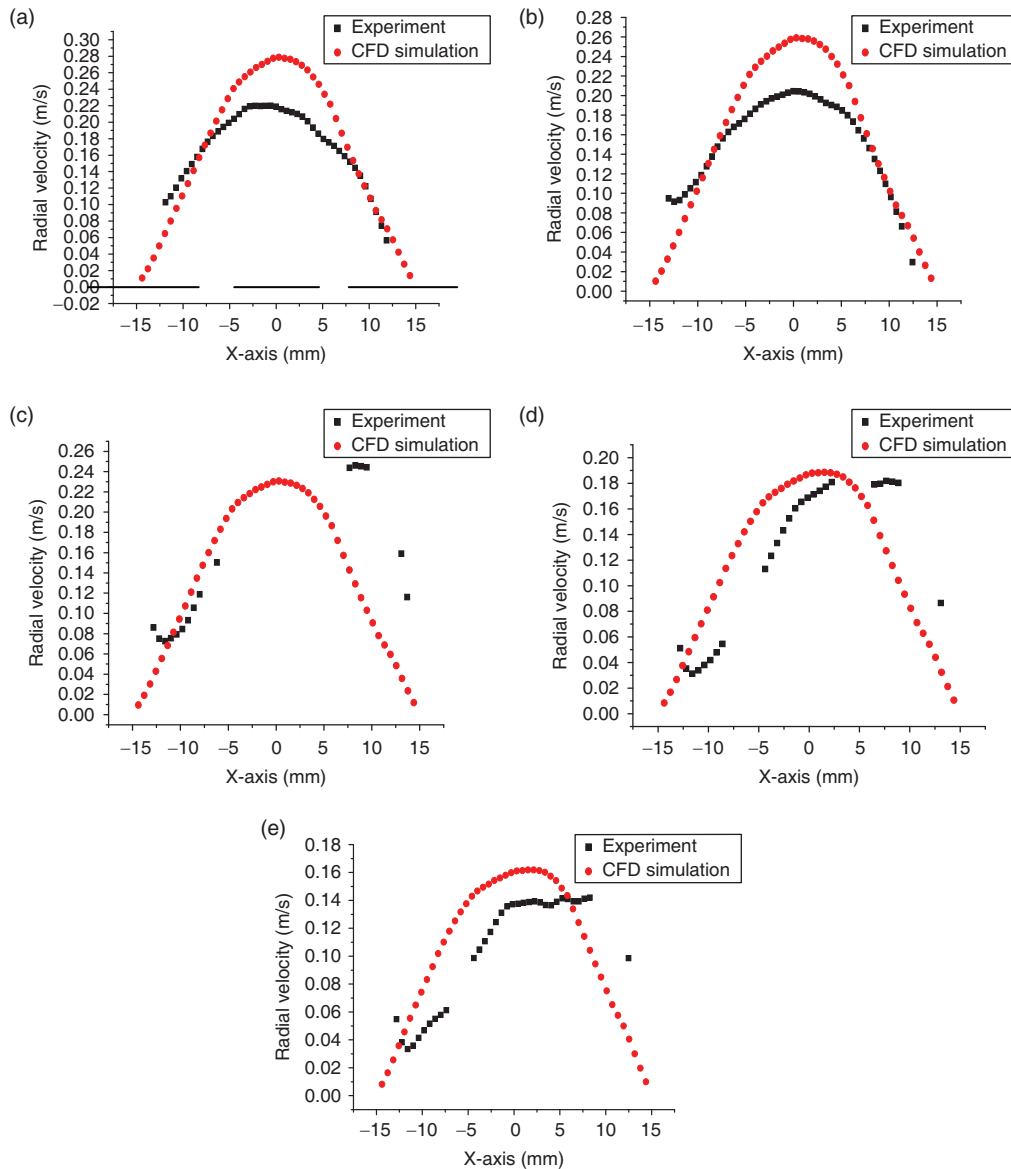


Figure 7. Comparison of the CFD Results and Experimental Data for Mean Radial Velocity of Air-Water Flow at the Z = -75 mm Axial Position; A: $1.96 \times 10^{-4} \text{m}^3/\text{s}$ (water), $4.5 \times 10^{-5} \text{m}^3/\text{s}$ (air); B: $1.85 \times 10^{-4} \text{m}^3/\text{s}$ (water), $4.5 \times 10^{-5} \text{m}^3/\text{s}$ (air); C: $1.58 \times 10^{-4} \text{m}^3/\text{s}$ (water), $4.5 \times 10^{-5} \text{m}^3/\text{s}$ (air); D: $1.48 \times 10^{-4} \text{m}^3/\text{s}$ (water), $4.5 \times 10^{-5} \text{m}^3/\text{s}$ (air); E: $1.32 \times 10^{-4} \text{m}^3/\text{s}$ (water), $4.5 \times 10^{-5} \text{m}^3/\text{s}$ (air).

$$\eta = \eta_c (1 + 2.5 \phi) \tag{10}$$

Where η is the viscosity of the dispersion, η_0 is the viscosity of the continuous phase and ϕ is the volume fraction of the dispersed phase. For example, at volume fraction of 18% the viscosity of the dispersion is calculated to be 0.00145 kg/ms. The CFD simulation used the viscosity of water flow (0.001003 kg/ms) instead of the dispersed system (Say 0.00145 kg/ms at volume fraction of 18 %). For multiphase flow, Einstein equation shows that an increase in viscosity leads to smaller velocity gradient with one layer of fluid flowing relative to another. Therefore, the predicted velocity profiles are exceptional high due to small viscosity of water flow by a factor of about 0.45.

(4) The systematic uncertainty of the SPIV measurement is calculated to be 0.11 m/s and observed to be higher than the random uncertainties. This is majorly responsible for the variation in the computed velocity magnitudes when compared with measured profile [14].

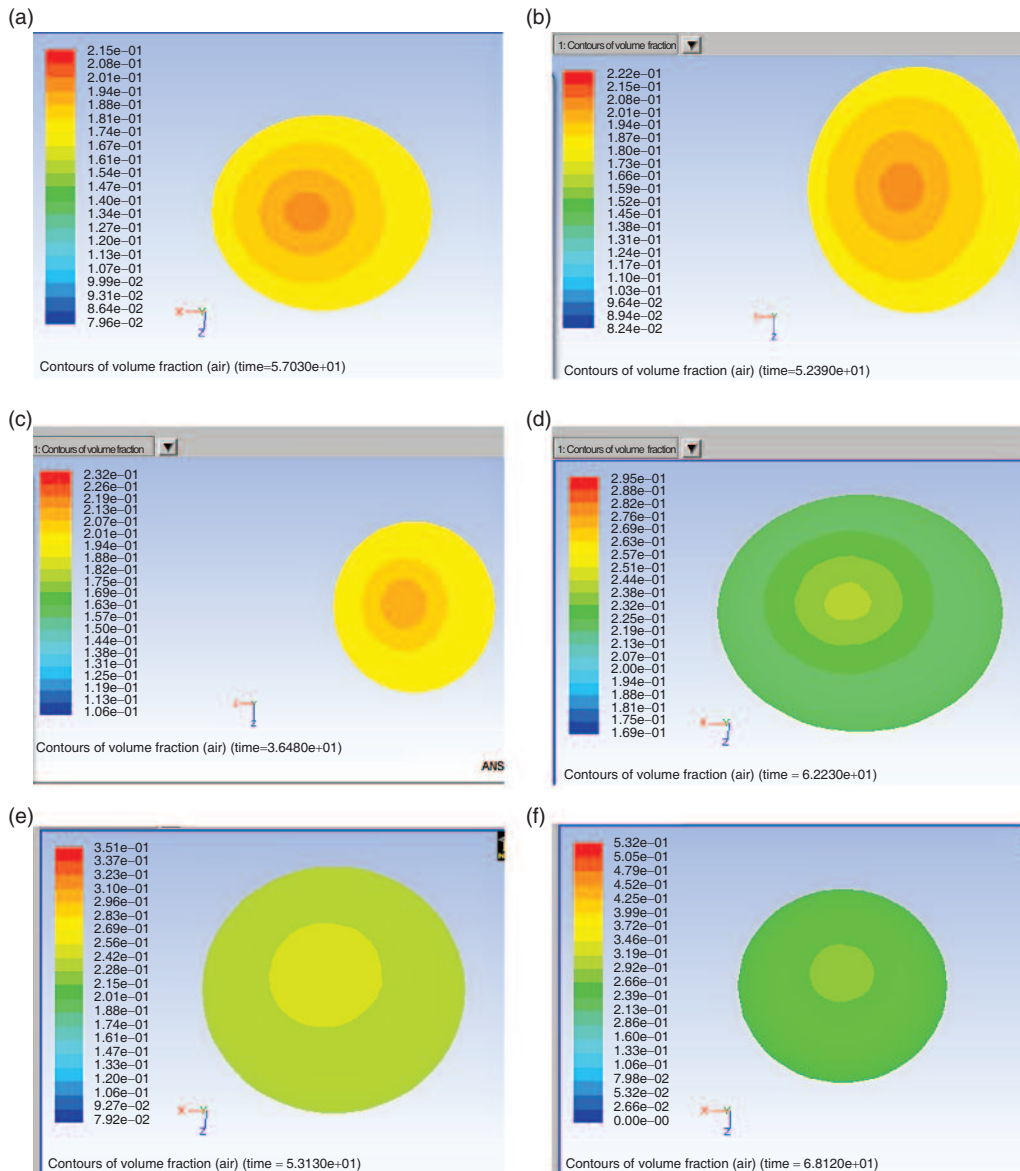


Figure 8. Contours of the Air Volume Fraction at the $Z = 295$ mm Axial Position; A: $2.05 \times 10^{-4} \text{m}^3/\text{s}$ (water), $4.5 \times 10^{-5} \text{m}^3/\text{s}$ (air); B: $1.96 \times 10^{-4} \text{m}^3/\text{s}$ (water), $4.5 \times 10^{-5} \text{m}^3/\text{s}$ (air); C: $1.85 \times 10^{-4} \text{m}^3/\text{s}$ (water), $4.5 \times 10^{-5} \text{m}^3/\text{s}$ (air); D: $1.58 \times 10^{-4} \text{m}^3/\text{s}$ (water), $4.5 \times 10^{-5} \text{m}^3/\text{s}$ (air); E: $1.48 \times 10^{-4} \text{m}^3/\text{s}$ (water), $4.5 \times 10^{-5} \text{m}^3/\text{s}$ (air); F: $1.32 \times 10^{-4} \text{m}^3/\text{s}$ (water), $4.5 \times 10^{-5} \text{m}^3/\text{s}$ (air).

- (5) The SPIV measurements used to validate the CFD results involved 200 images per camera captured by the high speed camera over a period of 4 minutes and then ensemble-averaged. However, it was too computationally demanding to carry out a 4 minutes transient simulation via the RSM and Eulerian methodology. As such, the difference in the timescale is a major factor for the poor quantitative agreement between the CFD results and the experimental data.

4. CONCLUSION

The comparisons between the predicted results and experimental data showed that:

- (1) The shape of the tangential velocity profiles appeared to be properly modelled at all axial positions, but the predicted tangential velocity magnitudes were either over-predicted or under-predicted. At $Z = -395$ mm, the magnitude of the tangential velocity profile is

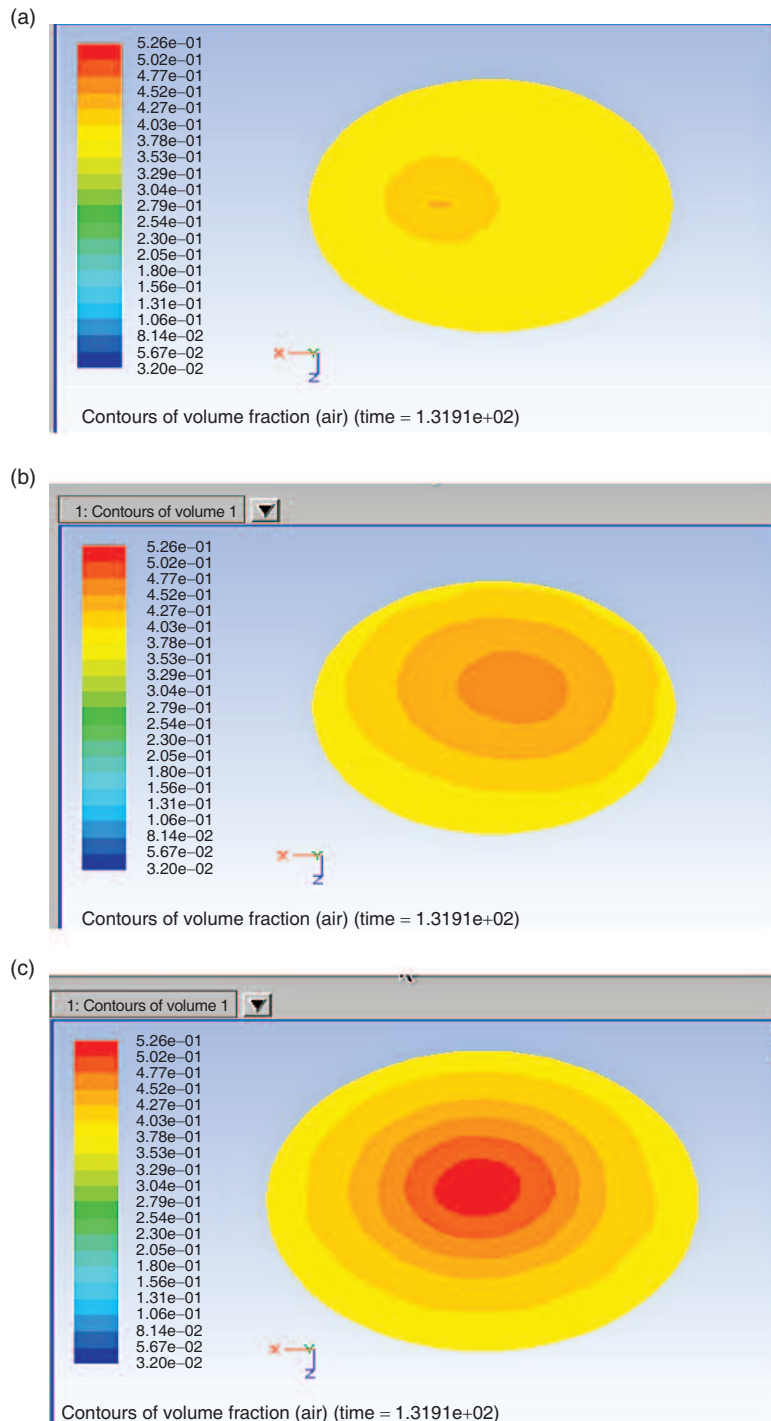


Figure 9. Contours of the Air Volume Fraction at the Axial Position of:
 (A) $Z = -395 \text{ mm}$ (B) $Z = -75 \text{ mm}$ (C) $Z = 295 \text{ mm}$.

found to be over-predicted close to the wall and under-predicted at the centre of the tube (Figure 2). However, it is under-predicted at most of the x-axis coordinates (Figure 3).

- (2) The general shape of the axial velocity profiles was predicted correctly at $Z = -75 \text{ mm}$, but the magnitudes of the predicted axial velocity were consistently computed close to the wall especially for small flow rates (Figure 4). At the centre of the tube, the CFD results were found to be over-predicted at high flow rates and under-predicted as flow rate decreases (Figures 4). However there is disagreement in the qualitative analysis at $Z = -395 \text{ mm}$. The computational

models failed to predict the upward flow pattern at the centre of the tube. ANSYS FLUENT under-predict the magnitude of the axial velocity at most of all x-axis coordinates.

- (3) The flow pattern of the radial velocity was correctly predicted at $Z = -75$ mm with the computed radial velocity magnitudes over-predicted at the centre of the tube, but the radial velocity magnitude was observed to be reducing with a decrease in the inlet flow rates. As we move close to the wall, the magnitude of the radial velocity was observed to be under-predicted at high flow rate, but over-predicted at small flow rates (Figure 6) At $Z = -395$ mm, the qualitative analysis showed that the predicted and measured results were not the same (Figure 5).
- (4) The measured and predicted results show retardation of the velocity near the walls and this satisfy no slip boundary conditions at the wall of the pipe separator.
- (5) The CFD results confirmed the presence of air core at the centre of the cross section and the magnitude of this air void fraction increases with an increase in the air volume fraction at the inlet (Figure 8 and 9). This confirmed the reason why fewer SPIV data are recorded at $Z = 295$ mm.

We can then conclude that RSM in conjunction with Eulerian model are good options for the numerical simulation of air-water flow in a pipe separator. This is true as the computational models were able to capture the basic patterns of flow in a pipe separator.

ACKNOWLEDGMENT

This research has been supported by the PTDF, Nigeria.

NOMENCLATURE

| | |
|---------------|---|
| p | Pressure (N/m^2) |
| t | Time (s) |
| V | Volume (m^3) |
| η | Viscosity of the dispersion (m^2/s) |
| p, q | Primary and secondary phase respectively |
| ρ | Density (kg/m^3) |
| α | Volume fraction (dimensionless) |
| τ_{ij} | Surface stress tensor (Pa) |
| τ_{ij}^p | Phase stress-strain tensor (Pa) |
| K_{dc} | Drag Coefficient |
| R_{ij} | Reynolds stress (Pa) |
| U | Velocity (ms^{-1}) |
| u' | Fluctuating velocity (ms^{-1}) |
| \bar{c} | Relative velocity (ms^{-1}) |
| v | Slip velocity (ms^{-1}) |
| δ_{ij} | Kronecker delta |
| ϕ | General scalar variable |

ACRONYMS AND ABBREVIATIONS

| | |
|--------------|---|
| PIV | Particle image velocimetry |
| LES | Large eddy simulation |
| $k-\epsilon$ | Turbulence model |
| RANS | Reynolds-averaged Navier Stokes |
| RSM | Reynolds stress model |
| RNG | Renormalization group ($k-\epsilon$ model variant) |
| SPIV | Stereoscopic particle image velocimetry |

REFERENCES

- [1] Vazquez, C. O, *Multiphase flow separation in Liquid-Liquid cylindrical cyclone and Gas-Liquid-Liquid cylindrical cyclone compact separators*, PhD Thesis, The University of Tulsa, 2001.
- [2] Delgadillo, J. A. and Rajamani, R. K, Computational fluid dynamics prediction of the air-core in hydrocyclones , *International Journal of Computational Fluid Dynamics*, 2009, 23, (2), 189–197.

- [3] Delgadillo, J. A. and Rajamani, R. K, Exploration of hydrocyclone designs using computational fluid dynamics, *International Journal of Mineral Processing*, 2007, 84, (1-4), 252–261.
- [4] He, P, Salcudean, M. and Gartshore, I. S, A numerical simulation of hydrocyclones, *Chemical Engineering Research & Design*, 1999, 77, (A5), 429–441.
- [5] Chine, B. and Concha, F, Flow patterns in conical and cylindrical hydrocyclones, *Chemical Engineering Journal*, 2000, 80, (1-3), 267–273.
- [6] Cullivan, J. C., Williams, R. A. and Cross, C. R, Understanding the hydrocyclone separator through computational fluid dynamics, *Chemical Engineering Research and Design*, 2003, 81, (4), 455–466.
- [7] Cullivan, J. C, Williams, R. A, Dyakowski, T. and Cross, C. R, New understanding of a hydrocyclone flow field and separation mechanism from computational fluid dynamics, 2004, *Minerals Engineering*, 17, (5), 651–660.
- [8] De Souza, F. J. and Neto, A. S, Large eddy simulations of a hydrocyclone, Proceedings of FEDSM 2002, *American Society of Mechanical Engineers, Fluids Engineering Division (Publication) FED*. Montreal, Que., 2002.
- [9] Brennan, M. S., Narasimha, M. and Holtham, P. N, Multiphase modelling of hydrocyclones prediction of cut-size, *Minerals Engineering*, 2007, 20, (4), 395–406.
- [10] Crowe, C.S., M; Tsuji, Y (1998) '*Multiphase flows with droplets and particles*' London CRC Press.
- [11] Lim, E.W, Chen, Y-Ren, Wang, C.H and Wu, R.M, W, Experimental and Computational Studies of Multiphase Hydrodynamics in a Hydrocyclone Separator System, *Chemical Engineering Science*, 2010, 65, 6415–6424.
- [12] Cokljat, D., Slack, M., Vasquez, S. A., Bakker, A. and Montante, G, Reynolds-stress model for Eulerian multiphase', *Progress in Computational Fluid Dynamics*, 2006, 6, (1-3), 168–178.
- [13] Afolabi, E.A and Lee J.G.M (2013). Stereoscopic particle image velocimetry analysis of air-water flow in a pipe separator, *International Review of Chemical Engineering (IRECHE)*, 2013, Vol.5.N.3, 6–16.
- [14] Afolabi, E.A, *Experimental Investigation and CFD Simulation of Multiphase flow in a Three Phase Pipe Separator*, Ph.D Thesis, Newcastle University, UK, 2012.
- [15] Slack, M. D., Prasad, R. O., Bakker, A. and Boysan, F, Advances in cyclone modelling using unstructured grids, *Chemical Engineering Research and Design*, 2000, 78, (8), 1098–1104.
- [16] Dyakowski, T. and Williams, R. A, Modelling turbulent flow within a small diameter hydrocyclone, *Chemical Engineering Science*, 1993, 48, (6), 1143–1152.
- [17] Launder, B. E. and Spalding, D. B, The numerical computation of turbulent flows', *Computer Methods in Applied Mechanics and Engineering*, 1974, 3, (2), 269–289.
- [18] Patterson, P. A. and Munz, R. J, Cyclone collection efficiencies at very high temperatures, *The Canadian Journal of Chemical Engineering*, 1989, Vol. 67, 321–328.
- [19] Utikar, R., Darmawan, H., Tade, M., Li, Q., Evans, G., Glenney, M. and Pareek, V, Hydrodynamic Simulation of Cyclone Separators Computational Fluid Dynamics, 2010, Book edited by: Hyoung Woo OH, ISBN 978-953-7619-59-6, www.intechopen.com.
- [20] Huang, S, Numerical simulation of oil-water hydrocyclone using Reynolds-stress model for Eulerian multiphase flows', *Canadian Journal of Chemical Engineering*, 2005, 83, (5), 829–834.
- [21] Bai, Z. S., Wang, H. I. and Tu, S. T, Experimental study of flow patterns in deoiling hydrocyclone, *Minerals Engineering*, 2009, 22, (4), 319–323.
- [22] Bergström, J. and Vomhoff, H, Experimental hydrocyclone flow field studies', *Separation and Purification Technology*, 2007, 53, (1), 8–20.
- [23] Leeuwener, M. J. and Eksteen, J. J, Computational fluid dynamic modelling of two phase flow in a hydrocyclone, *Journal of The South African Institute of Mining and Metallurgy*, 2008, 108, (4), 231–236.
- [24] Erdal, F. M, *Local Measurements and Computational Fluid Dynamic Simulations in a Gas-Liquid Cylindrical Cyclone Separator*, Ph.D, the University of Tulsa, 2001.
- [25] Tu, J, Yeoh, G.H, and Liu, C, *Computational Fluid Dynamics: A Practical Approach First edition*, Elsevier Inc. Oxford, UK, 2008.
- [26] Versteeg, H. K. and Malalalsekera, W, *An introduction to computational fluid dynamics: the finite volume method*, Harlow Prentice Hall, 2007.
- [27] Coupland, J, Food Chemistry Course Materials, (FDSC 400)', website for fall 2004 https://www.courses.psu.edu/fd_sc/fd_sc400_jnc3/dispersion/3Ddispersed%20systems.pdf

